Automotive and Engine Technology (2026) 11:3
https://doi.org/10.1007/s41104-025-00165-7

RESEARCH

Numerical simulation and experimental validation of NO emissions in a heavy-duty H_2DI engine considering injector needle dynamics and multi-cycle analysis

Marcel Reinbold[1] · Mingyi Liang[2] · Manuel Bucherer[1] · Sameera Wijeyakulasuriya[2] · Thai An Bui[1] · Kelly Senecal[2] · Thomas Koch[1]

Received: 19 November 2025 / Accepted: 15 December 2025

Abstract

Hydrogen direct-injection engines offer a promising pathway for decarbonizing heavy-duty transportation, but accurate prediction of mixture formation and NO_x emissions remains challenging due to complex injector dynamics and strong cycle-to-cycle variability. This work presents a comprehensive computational and experimental investigation of supersonic H_2 direct injection, mixing, combustion, and NO formation in a single-cylinder heavy-duty hydrogen engine operated at 1100 rpm and $\lambda = 2.6$. A detailed three-dimensional CFD model is developed, coupling a pressure-based injection boundary condition with a realistic *Bosch* F2 prototype injector needle-lift profile to capture valve-bounce effects. The model is validated against measured in-cylinder pressure, fuel and air mass, and NO emission data. Multi-cycle combustion behavior and NO emission variability are analyzed using the concurrent perturbation method (CPM), with 20 statistically independent realizations at reduced computational cost. Results show that near-spark mixtures with higher fuel concentration accelerate flame propagation and increase peak NO by a factor of two (76 ppm vs. 32 ppm). Simulations reveal that NO forms predominantly in local pockets of high fuel concentration, with turbulent flame speeds of 11–22 m/s during the early combustion phase. Predicted exhaust-port NO levels agree qualitatively with experiments, though unsteady RANS tends to overpredict NO due to limited small-scale mixing. The study demonstrates that resolving the injector flow rather than approximating boundary conditions, combined with CPM can effectively capture hydrogen combustion dynamics and emission variability.

Keywords H2DI · Mixing · CCV · CPM · NO formation · CFD

Marcel Reinbold and Mingyi Liang contributed equally to this work and are co-first authors.

✉ Marcel Reinbold
marcel.reinbold@kit.edu

Mingyi Liang
mingyi.liang@convergecfd.com

Manuel Bucherer
manuel.bucherer@kit.edu

Sameera Wijeyakulasuriya
sameera.wijeyakulasuriya@convergecfd.com

Thai An Bui
thai.bui@student.kit.edu

Kelly Senecal
senecal@convergecfd.com

Thomas Koch
thomas.a.koch@kit.edu

[1] Karlsruhe Institute of Technology, Karlsruhe, Germany

[2] Convergent Science, Madison, USA

Published online: 08 January 2026

1 Introduction

Addressing the pressing challenge of reducing carbon dioxide (CO_2) emissions is critical to mitigating global warming. The global objective, as outlined in the Paris Agreement, is to limit the rise in global average temperature to 1.5 K above pre-industrial levels. Achieving this requires greenhouse gas emissions to peak no later than 2025 and to decrease by 43% by 2030, ultimately reaching net-zero emissions by the middle of the century. These targets underscore the need for immediate and substantial emission reductions across all sectors of society [1, 2].

Road transportation, which contributes roughly 25% of CO_2 emissions in the EU, holds a pivotal role in this transition. In particular, heavy-duty vehicles such as trucks and buses emitted 206.5 million metric tons of CO_2 in 2021, accounting for 27% of the EU's road traffic emissions [3].

Green hydrogen, derived from renewable energy sources, represents a promising avenue for decarbonizing the energy system while reducing reliance on finite resources. Incorporating green hydrogen into spark-ignited internal combustion engines (ICEs) offers a practical approach to lowering the carbon footprint of future vehicles. Hydrogen-powered ICEs deliver high power output, cost-efficient operation, and robust, reliable performance, making them especially well-suited for heavy-duty applications [4].

A crucial aspect of hydrogen combustion in ICEs is the fuel injection process and its impact on mixture formation. Poor mixing can create pockets of high fuel concentration near the spark plug, which promotes high NO formation during combustion. Therefore, achieving a homogeneous mixture is critical for low emissions. However, modeling hydrogen injection presents significant challenges due to the characteristics of gaseous fuel injectors, which have large valve lifts and relatively slow opening and closing dynamics. The injector in the present study also includes injector valve bounce during closing. Accurately capturing these transient effects is essential for reliable predictions of mixture formation and combustion behavior [5].

Former studies regarding hydrogen injection in engines have already been conducted by various researchers. Wu et al. [6] conducted CFD simulations to analyze hydrogen direct injection (DI) in an optical research engine, investigating the impact of in-cylinder flow patterns on fuel-air mixture preparation under high-pressure conditions. Their results highlight the importance of turbulence modeling and the turbulent Schmidt number in accurately predicting hydrogen mixing and combustion characteristics. Zareei et al. [7] simulated a hydrogen/natural gas direct injection engine, demonstrating that adding hydrogen improves engine performance by increasing power and efficiency while reducing specific fuel consumption and CO emissions. Their model validation against experimental data confirmed a strong correlation, with an optimal hydrogen percentage and ignition timing identified for enhanced combustion. Scarcelli et al. [8] developed a 3D-CFD model for hydrogen direct injection engines, validated against laser-based measurements, to study mixture stratification and combustion stability. Their findings show that injection timing and direction significantly influence fuel-air mixing, with stable combustion achieved when the injector is aimed towards the spark plug. Babayev et al. [9] investigated hydrogen direct injection compression ignition (DICI) using CONVERGE®, revealing that hydrogen jets exhibit a highly stratified fuel-air interface with minimal premixing. Their study emphasizes the dominance of free-jet mixing over global mixing, necessitating new optimization strategies for hydrogen CI engines. Sukumaran et al. [10] developed a hybrid gas jet injection model with adaptive mesh refinement to simulate high-velocity hydrogen injection and in-cylinder mixing. Their results show that early injection near the intake valve promotes better mixture homogeneity by leveraging intake flow interactions for enhanced fuel-air mixing.

All previous studies utilized mass-flow boundary conditions for hydrogen injection modeling, simplifying the transient injector dynamics by prescribing a simplified predefined mass flow rate. In contrast, the present study employs a pressure boundary condition combined with measured needle lift data to model the injection process, explicitly capturing the mass flow changes due to the motion of the injector valve. This approach enables a more accurate representation of the transient injection dynamics, including the injector valve's bouncing effect, where the valve does not seal immediately upon closing but momentarily reopens after impacting the valve seat before fully closing. By incorporating these effects, the present study aims to provide a more comprehensive understanding of hydrogen injection and mixture formation. Furthermore, an accurate injection model is essential when involving NO_x emissions, as these are also investigated in the present work and are highly sensitive to local regions of high fuel concentrations near the injector, which can be influenced by valve bouncing effects and the following air-H_2 mixing process.

Capturing cycle-to-cycle variability (CCV) in internal combustion engines is essential for accurately predicting real engine behavior, particularly in the presence of turbulence-driven mixture inhomogeneities and combustion instabilities. However, traditional multi-cycle simulations are computationally expensive due to the need to run each cycle consecutively. To address this, the concurrent perturbation method (CPM), originally proposed by Ameen et al. [11], is adopted. CPM is a promising approach for efficiently simulating multiple engine cycles for engine operating points that do not exhibit cycle to cycle coupling. By

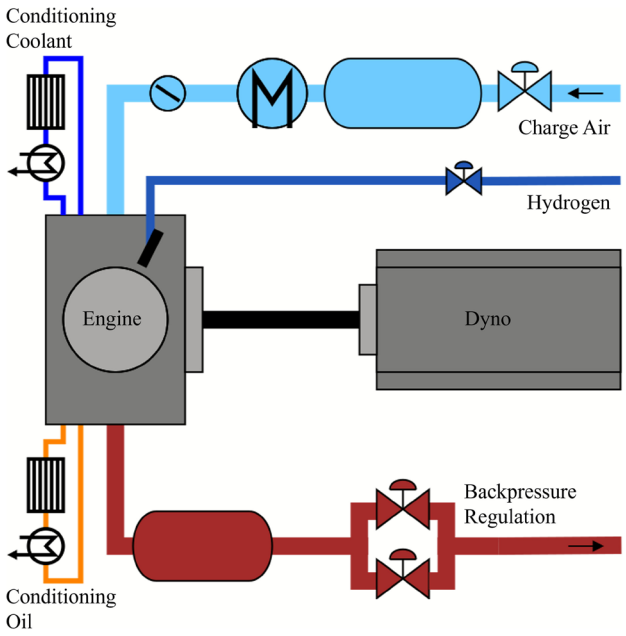

Fig. 1 Schematic single-cylinder test bench setup [13]

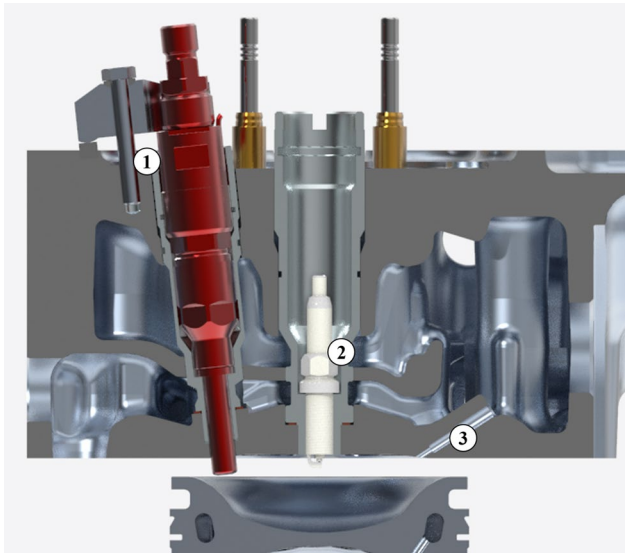

Fig. 2 Cut section view of direct injection setup with a lateral *Bosch* F2 HIDI hydrogen injector (1), a central spark plug (2) and the pressure sensor access point (3) visible [13]

initializing each cycle from a common baseline and introducing small perturbations to the velocity field inside the intake port, CPM allows for the concurrent execution of individual cycles, significantly reducing computational cost while preserving the physical cyclic variability of combustion. Its effectiveness has been validated by Probst et al. [12], who showed that concurrently simulated cycles yield statistically meaningful CCV results comparable to those of conventional consecutive-cycle simulations. Although CPM has been applied to gasoline and natural gas engines, its use in hydrogen-fueled internal combustion engines (H_2ICE) has not yet been explored. This study therefore investigates the applicability of CPM in the context of H_2ICE operation.

2 Engine and test bench setup

The experimental data presented in this study was obtained using the test bench facilities at the Institute of Internal Combustion Engines (IFKM), Karlsruhe Institute of Technology (KIT), which employs a single-cylinder engine modeled after the Volvo D13 cylinder design.

Figure 1 provides a schematic overview of the test bench configuration. The central charge air system includes air conditioning and pressure regulation features, with a throttle valve for idle load operation. The intake airflow is measured using a rotary gas meter.

To include the effects of a turbocharger, the exhaust back pressure of the engine is actively regulated by two control valves. The test bench also includes standard exhaust measurement systems capable of analyzing O_2, CO, CO_2, HC, and NO_x, augmented by a mass spectrometer to detect residual hydrogen (H_2) in the exhaust. A Fast-NO measurement system provides high-resolution NO emission data. Intake, exhaust, cylinder, and rail pressures are recorded using a dedicated indication system with a resolution of 0.1 °CA.

The hydrogen injection system is supplied from an external 300-bar reservoir and provides pressures up to 50 bar. The hydrogen rail is equipped with a pressure sensor located approximately 30 cm upstream of the injector tip. The fuel consumption of the engine is monitored using a Coriolis flow meter. For the experiments in this work, direct injection was used exclusively. Due to the engine's low inherent charge motion, the hydrogen jet is a key factor in the mixture formation process.

The cylinder head was modified to accommodate an M12 central spark plug and a lateral hydrogen direct injector. The hydrogen injector used was a *Bosch* F2 HIDI, an early prototype of a low pressure direct injector (operated at 15 bar rail pressure in this work). A cut section view of the cylinder head assembly, including the lateral injector, the central spark plug and the piston in top dead center, is shown in Fig. 2. The injector can be fitted with different jet forming caps to adjust the form of the hydrogen jet and improve mixture formation and homogenization. For the experiments shown in this work, a jet forming cap (Fig. 3) with a central single 6.4 mm-diameter hole was used.

To mitigate the limited cooling capacity of the diesel-based cylinder head in hydrogen applications, a relatively low compression ratio of 9.5 was selected. To achieve this, the piston was machined from an aluminum blank and designed with a spherical bowl. Detailed engine

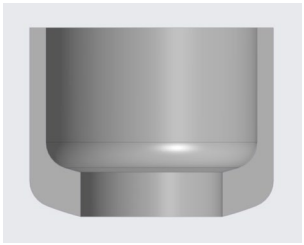

Fig. 3 Cut section view of the used single hole jet forming cap with a central hole and hole-diameter of 6.4 mm [13]

Table 1 Specification of the used single-cylinder engine

Displacement	2166	cm^3
Stroke	157	mm
Bore	131	mm
Conrod length	275	mm
Compression ratio	9.5:1	

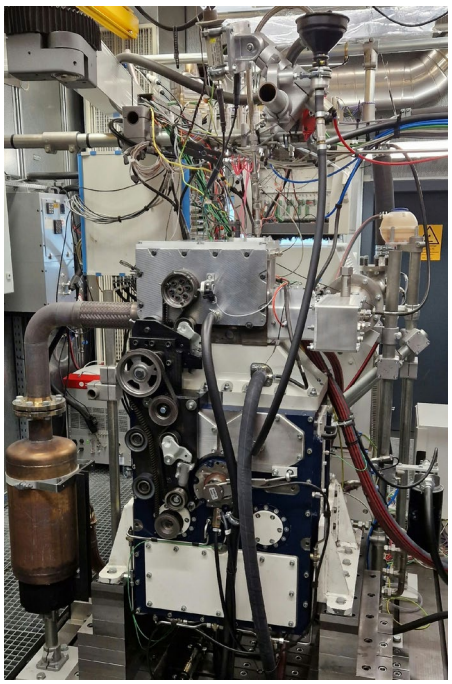

Fig. 4 Single-cylinder engine on the test bench at IFKM [13]

Table 2 Operating point specifications

IMEP	8.0 bar
λ	2.6
RPM	1100 1/min
Fuel mass	1.183 kg/h
Intake air mass	105.9 kg/h
Covariance IMEP	0.8%
Start of energizing (SOE)	−180 °CA
Ignition timing	−11 °CA
Rail pressure	15 bar

specifications can be found in Table 1. This choice helps to prevent irregular combustion and enables experiments across wide areas of the engine map.

A picture of the final engine setup can be seen in Fig. 4. It shows the custom belt drive that was fitted to ensure compatibility with the cylinder head's single overhead camshaft configuration.

The investigated operating conditions are listed in Table 2. This specific point was chosen as it represents a typical highway cruising scenario for commercial vehicles and allows for a broad variation of control parameters based on an extensive existing database at the test facility. For all crank-angle-resolved measurements, the test bench records both the mean values averaged over 200 consecutive engine cycles and the corresponding individual cycle data. For all other measurement signals, a time-based averaging window of 30 s is applied.

3 Experimental H_2 injection data

Accurately modeling the hydrogen injection process presents significant challenges due to the dynamics of the H_2 injector valve. Unlike conventional diesel or gasoline injectors, large lift is needed for gas-phase injectors, since the mass flow rate is significantly lower [14]. Moreover, the actuation time of a hydrogen injector does not directly correspond to its actual opening duration due to inherent delay times, due to the mechanical inertia of the injector valve and its relatively large lift.

In Fig. 5, the rail pressure signal and the injection current of the actuation used in this study are compared. Note that all crank angle specifications in this work are referenced to the top dead center (TDC) at which combustion occurs. A negative sign indicates that the measured crank angle is before firing.

The comparison clearly reveals the discrepancy between the electrical actuation of the injector and the actual lift of the injector valve. At −180 °CA (crank angle degrees), the injection current starts to increase. 9 °CA later, the pressure in the hydrogen rail begins to decrease. At injector closing, a discrepancy of 8.5 °CA is observed between the point at which the injection current drops to zero and the crank angle at which the rail pressure reaches its local maximum, indicating a momentarily closed injector needle. Given that the pressure signal must travel approximately 30 cm from the injector to the upstream measurement location, as discussed in Sect. 2, a correction of 1.5 °CA needs to be accounted for the signal propagation time, assuming it travels at the speed of sound. A closer examination of the pressure signal at −140 °CA and beyond reveals that after the initial closing attempt of the valve, it reopens and closes multiple times

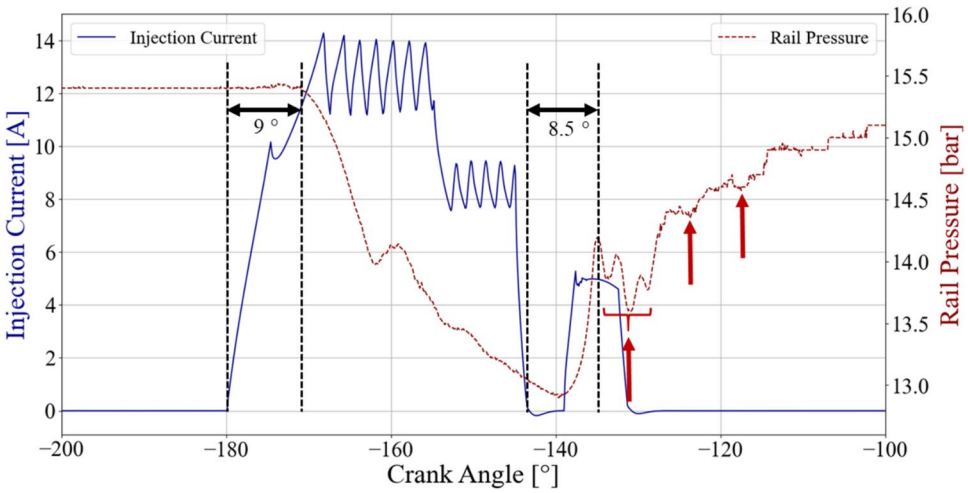

Fig. 5 Injection current and rail pressure over crank angle. The left y-axis represents the injection current in amperes (A) and the right y-axis shows the rail pressure in bar

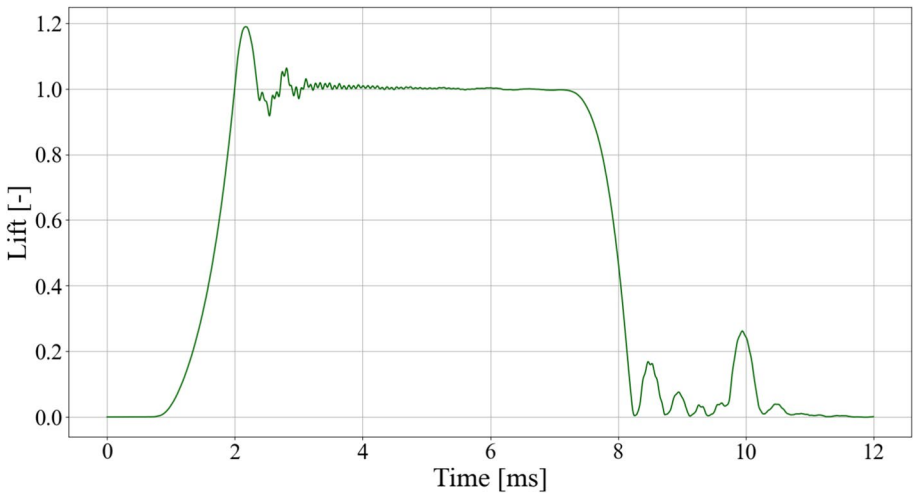

Fig. 6 Dimensionless valve lift over time for the F2 hydrogen injector, provided by the manufacturer *Bosch*

("valve bouncing"), as indicated by the alternating increase and decrease in pressure. The red arrows in Fig. 5 highlight these events, with the last red arrow indicating the crank angle at which the injector valve is fully closed and completely sealed.

Further confirmation of this effect is provided by the measured needle lift data from the manufacturer *Bosch*, showing the valve motion over time for an example injection event in Fig. 6.

The measured needle lift highlights the necessity of including detailed injector lift if a realistic representation of the hydrogen injection process needs to be achieved.

To do this, significant crank angles are extracted from the rail pressure signal measured at the test bench. For clarity, they are plotted in Fig. 7 without applying the offset due to the signal propagation time, providing a more intuitive understanding of the extraction strategy.

The first point on the red line in Fig. 7 marks the beginning of the hydrogen injector valve opening, as indicated by the decrease in pressure, signifying hydrogen mass leaving the injector. The second point, at −162 °CA, is considered the end of the opening phase, as a short pressure increase occurs when the valve momentarily exceeds its maximum lift before returning to this position. This behavior is illustrated in Fig. 7 by the red line, as the dimensionless valve lift exceeds 1 during the first opening. At −140 °CA, the pressure begins to rise again, indicating the start of the first closing. By −135 °CA, the valve is briefly fully closed before the first bounce occurs, instead of remaining sealed, resulting in a characteristic peak in the pressure signal. During the subsequent crank angle period, until −129 °CA, the valve remains open for a short duration due to the first bounce. At −129 °CA, the pressure rise suggests that the valve has closed again. A second, smaller bounce is observed as a temporary pressure drop, concluding at −124 °CA when the pressure increases once more. This pattern repeats one final time, and at −117.5 °CA, the valve is assumed to be fully closed and sealed, since the pressure rises continuously.

The events and corresponding crank angles are listed in Table 3, accounting for the 1.5 °CA offset due to signal propagation time.

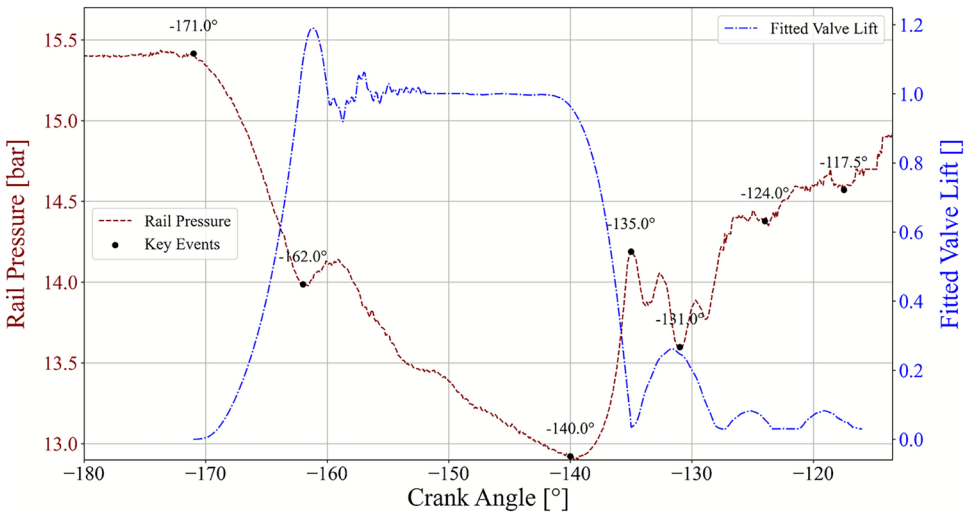

Fig. 7 Fitted dimensionless valve lift and rail pressure over crank angle

Table 3 Key events during the injection process with respect to an 1.5 °CA offset due to signal propagation time

Crank angle [°]	Event
−171.0 (−1.5)	Start of opening
−162.0 (−1.5)	End of opening
−140.0 (−1.5)	Start of first closing
−135.0 (−1.5)	End of first closing
−129.0 (−1.5)	End of closing after 1st bounce
−124.0 (−1.5)	End of closing after 2nd bounce
−117.5 (−1.5)	End of closing after 3rd bounce

As a first step of the injection modeling process, the original lift curve provided from *Bosch* is fitted to the crank angles listed in Table 3. To do this, the time in milliseconds from Fig. 6 is converted to crank angle degrees (°CA). The test bench engine in this study operated at 1100 rpm. The crank angle corresponding to the first nonzero valve lift is set equal to the first opening crank angle extracted from the measurement data (see Table 3). The end of the opening phase follows directly from the valve lift curve without further modifications. The start of the first closing event does not align with the example valve lift curve and therefore requires adjustment by correcting the duration of the fully opened valve state. This discrepancy arises because the valve lift curve provided by *Bosch* serves as an example and does not precisely correspond to the investigated operating point. In contrast, the end of the first closing phase naturally aligns with the valve lift curve. The injector valve bounce is modeled differently from the manufacturer's valve lift curve. Based on the measurement data, three pressure drops are observed after the initial valve closing. The first drop is more pronounced than the subsequent two, which are smaller in magnitude. Consequently, the valve lift curve includes a pronounced initial bounce followed by two smaller subsequent oscillations. Their magnitudes are scaled relative to the maximum lift, following the pattern observed in the example valve lift profile provided by *Bosch*. Figure 7 shows the resulting fitted valve lift curve along with the measured rail pressure.

As the final step, the pressure at the injector tip must be determined for the boundary condition for the numerical investigation. As discussed in Sect. 2, the pressure measurement is not taken directly at the injector tip but approximately 30 cm upstream. In addition to signal propagation time, there are pressure losses along the way. Since only the injector tip is included in the simulation, these losses must be accounted for setting up the pressure boundary condition. Under steady conditions, the pressure at the injector tip is approximately 80% of the measured pressure upstream, as specified by *Bosch*. At the initial stage of valve opening, the velocity within the rail and injector is nearly zero, suggesting that no pressure loss coefficient needs to be applied. As hydrogen starts flowing out of the injector and a steady-state flow develops, the steady pressure loss assumption becomes valid. The exact crank angle at which this transition from unsteady to steady flow occurs is difficult to determine. The flow is assumed to reach a quasi-steady condition when the pressure drop in the rail reaches its maximum. Between the onset of valve opening and this point, the pressure loss coefficient is modeled as a quadratic function of the crank angle. This is based on the quadratic dependence of pressure losses on flow velocity [15], in combination with the assumption of a linear relationship between velocity and time (or crank angle) during this phase. The pressure loss coefficient is set to zero at the beginning of the opening event and reaches a value of 0.8 at the point of maximum pressure drop.

The pressure applied at the injector tip (boundary condition) is obtained by multiplying the rail pressure with the corresponding pressure loss coefficient. Figure 8 illustrates this process, where the boundary pressure is derived as a function of the crank angle by combining the measured rail pressure with the pressure loss coefficient.

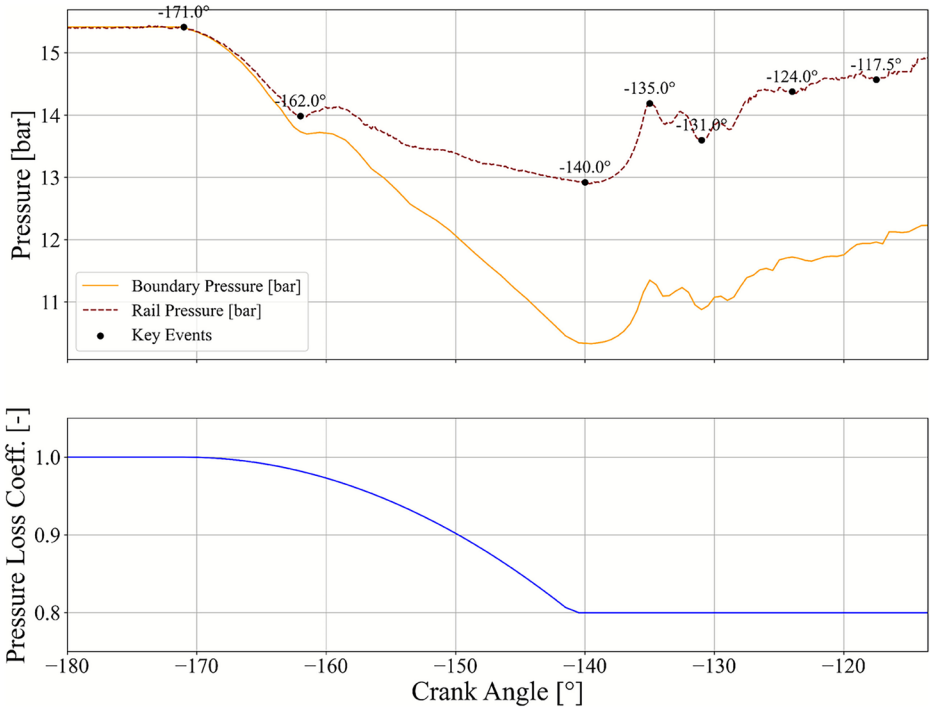

Fig. 8 Measured rail pressure, boundary pressure, pressure loss coefficient over crank angle

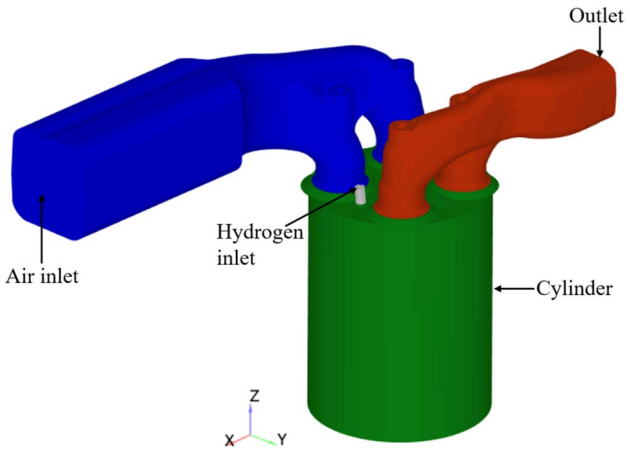

Fig. 9 Simulation domain colored by regions

4 Simulation setup and methodology

Numerical simulations are carried out using a widely used CFD software, *CONVERGE*® (version 4.1.2) [16]. The code uses a modified cut-cell Cartesian method to generate the mesh at runtime. An overview of simulation setup and methodology is discussed in this section.

4.1 Geometry, boundary conditions, and mesh

The simulation domain is shown in Fig. 9, highlighting the intake (blue), exhaust (red), cylinder (green), and hydrogen injector (grey) regions. Crank-angle-resolved measured pressure profiles are imposed at the air inlet, hydrogen inlet and exhaust outlet boundaries. The exhaust outlet has a Neumann boundary condition to account for any backflow that might occur. All other boundaries are treated as either moving or stationary walls with constant wall temperatures. The intake valves, exhaust valves, and the hydrogen injector valve, along with the piston, followed prescribed motion profiles which captured opening and closing times for valves which are listed in Table 4.

Table 4 Valve open and close timing

	Open(°CA)	Close(°CA)
Intake valve	329	573
Exhaust valve	117	367
H_2 valve	553	584
H_2 valve bounce	594	597

Figure 10 shows the measured valve lift for the H_2 injector and the profile used in the simulation. In the simulation, all valve bounces following the first hydrogen valve closing are consolidated into a single bounce at approximately 10 ms by summing their magnitudes. This is done to accurately account for the total mass of injected fuel at a low computational cost.

A summary of the thermal boundary conditions used in the simulation is provided in Table 5.

The computational mesh has a base cell size of 4 mm (the largest cell size in the domain) and is locally refined using fixed embeddings (up to level 6–0.0625 mm cell size) around critical components such as the intake and exhaust valves, cylinder volume, piston crevice, spark plug,

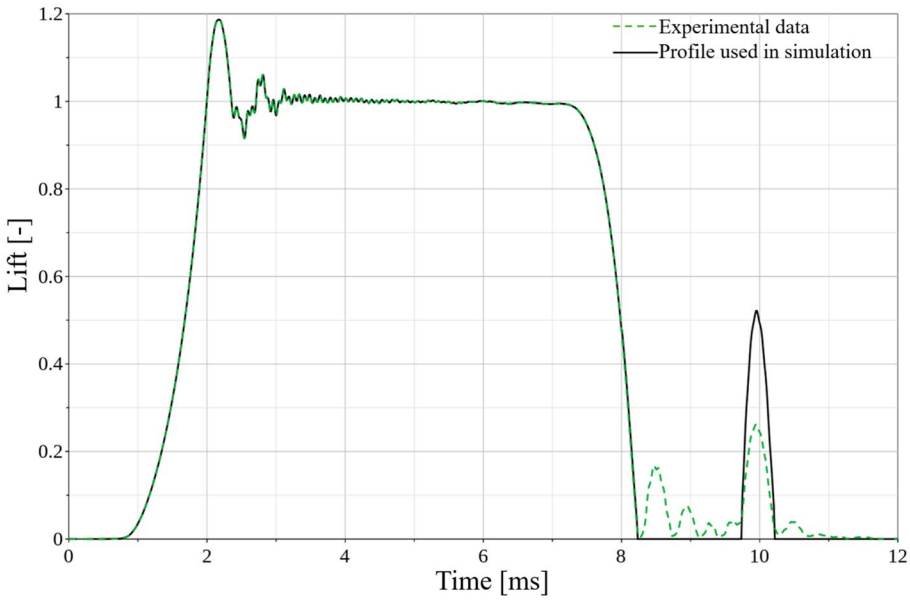

Fig. 10 Dimensionless valve lift over time for the H_2 injector, provided by the manufacturer *Bosch* and modified for the simulation

Table 5 Thermal boundary conditions

Boundary name	Temperature (K)
Engine head and piston wall	473
Piston crevice	353
Liner	383
Intake-port wall and valve surface	350
Exhaust-port wall and valve surface	400
Intake-valve bottom surface	380
Exhaust-valve bottom surface	420
Air inlet	308
H_2 inlet and valve surfaces	333
H_2 cap	400
H_2 port	353
Outlet	Neumann

and fuel injection region. Refinements near the spark plug and injector are activated only during the combustion and injection phases, respectively. Additionally, adaptive mesh refinement (AMR) is applied to dynamically refine the mesh in the intake, cylinder, and exhaust regions up to level 3 based on velocity (0.5 mm cell sizes) and level 4 based on temperature (0.25 mm cell sizes). Figure 11 shows the mesh during fuel injection and combustion, respectively with closeup view of the hydrogen injector valve and spark plug. The finest mesh resolution corresponds to a cell size of 0.0625 mm near the spark plug. The minimum and maximum total cell count in the simulation are approximately 0.8 million right before ignition and 10 million during combustion, respectively.

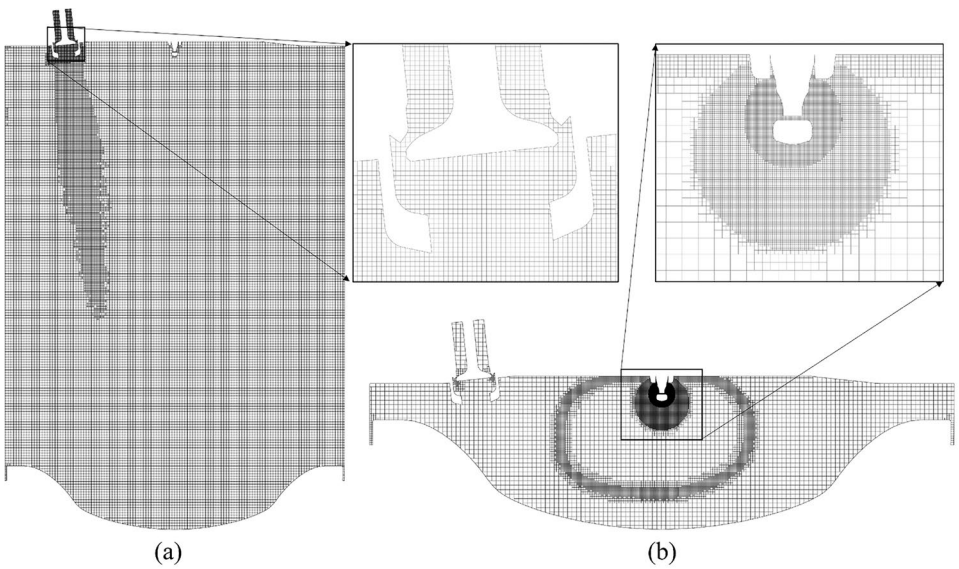

Fig. 11 Computational mesh at **a** cylinder center plane during hydrogen injection and **b** TDC

4.2 Physical models

Turbulence is modeled using the unsteady Reynolds-Averaged Navier–Stokes (URANS) approach in combination with the Renormalization Group (RNG) k-ϵ model [17]. The governing equations are discretized spatially using a second-order central scheme and temporally using a first-order implicit Euler scheme. Pressure–velocity coupling is handled using the Pressure-Implicit with Splitting of Operators (PISO) algorithm [18], and compressibility effects are accounted for by applying the Redlich–Kwong real-gas equation of state [19]. Wall heat transfer is treated using the model developed by O'Rourke and Amsden [20], and a standard wall function [21] is used for near-wall velocity predictions.

Combustion is modeled using the SAGE detailed chemistry solver with temperature and reaction-ratio used as adaptive zone binning dimensions [22]. H_2 and NO_x chemistry was extracted using the parent mechanism *C3MechV3.3* [23]. This extracted mechanism has 34 gas species and 242 chemical reactions. Reaction rates follow Arrhenius kinetics, incorporating species concentrations, stoichiometric coefficients, and temperature dependence [24]. The molecular mass diffusivity of each species is calculated using a mixture-averaged diffusion model that accounts for preferential species diffusion [25]. This is particularly important for accurately predicting H_2–air mixing.

4.3 Multiple cycle simulations

Multiple consecutive cycle simulations can be time-consuming. As an alternative, the concurrent perturbation method (CPM), originally proposed by Ameen et al. [11] and later validated by Probst et al. [12, 26], enables concurrent cycle simulations. These studies demonstrated that when there is no significant cycle-to-cycle coupling via internal residuals, which is typically absent under lean mixture or low back-pressure conditions that cause varying trapped residuals [27], running concurrent cycles starting at intake valve open (IVO) yields statistically meaningful results for engine CCV.

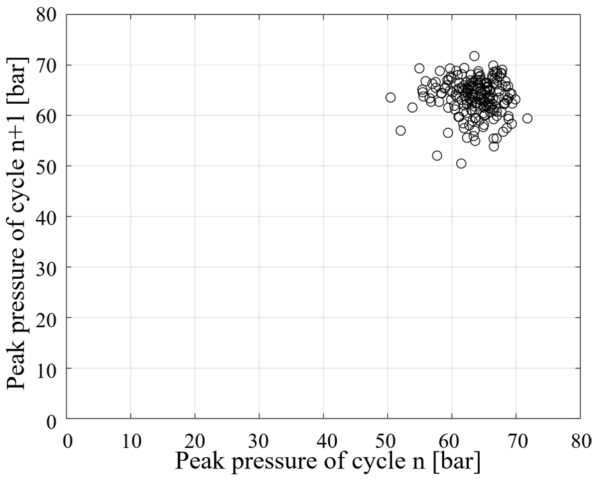

Fig. 12 Relationship between measured peak cylinder pressure of cycle n and cycle n+1

Cycle-to-cycle coupling was assessed in this study using return maps of measured crank-angle-resolved cylinder pressure over 200 consecutive cycles. The relationship between the peak pressures of cycle n and n+1 in Fig. 12 shows a random scatter with no discernible trends, indicating weak correlation between adjacent cycles. Therefore, CPM is appropriate for the present operating condition.

An isotropic velocity perturbation is applied to cells in the intake port region at IVO. The perturbation magnitude is 10% of the volume-averaged velocity inside the intake port at IVO, which is within reasonable range that can preserve the reliability of the simulation [26]. A random number seed was then used to generate different random perturbations for each cycle, based on the magnitude.

To the best of authors' knowledge, CPM has not been applied to simulate CCV of H_2ICE and this work is the first to demonstrate this usage.

4.4 Simulation run time

A normalized wall time of a typical engine cycle is shown in Fig. 13. The fuel injection process—including a main open-close event and a bounce—accounts for approximately 34% of the total wall time of a typical cycle, due to the high jet velocity and the small cell sizes required to resolve it. Immediately after exhaust valve opening (EVO), temperature- and velocity-based AMR is applied in the exhaust port to resolve steep flow variations around the valves. As the high-temperature, high-velocity flow enters the port, the cell count continues to increase, which accounts for approximately 43% of the total wall time of a typical engine cycle. After around 200 °CA, the variations smooth out, the mesh coarsens, and the simulation proceeds more efficiently. The long simulation time is also attributed to the stringent Courant–Friedrichs–Lewy (CFL) number constraint and the continuous activation of the combustion model in the exhaust port. In typical engine simulations, the velocity-based CFL number is limited to 1 during intake, compression, and combustion, and relaxed to 5 during the exhaust stroke. The combustion model is usually restricted to the combustion chamber and active only during the combustion period. However, in this study, the CFL number was maintained at 1 and the combustion model remained active throughout the entire cycle to ensure continued NO production during exhaust stroke as well.

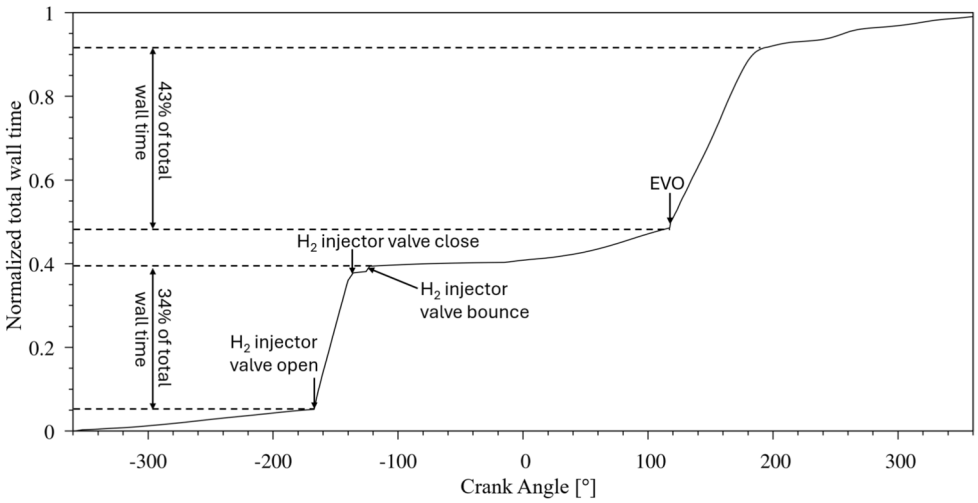

Fig. 13 Normalized total run time for a typical hydrogen engine cycle, simulated in this study

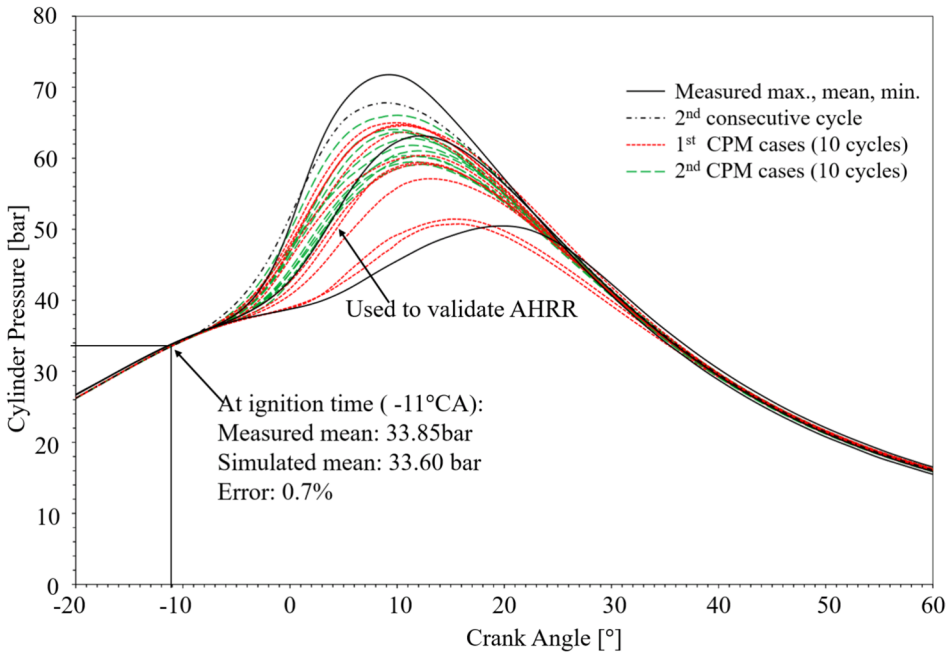

Fig. 14 Cylinder pressure results from measurements, consecutive cycles, and CPM cases

5 Results

5.1 Model validation

The results of 22 cycles are discussed in this section: 2 consecutive cycles and 20 CPM cycles to predict CCV.

Experimentally-measured inlet masses are 3.21 *g* of air and 0.0358 *g* of hydrogen per cycle. Based on the prescribed inlet pressure profiles, 3.26 *g* of air and 0.0364 *g* of hydrogen are predicted to enter the cylinder in the first simulated cycle, corresponding to errors with respect to the experimental results of 1.7% and 1.4%, respectively. After the initial conditions are washed away, the second simulated consecutive cycle and all 20 concurrent cycles yield 3.19 *g* of air and 0.0364 *g* of hydrogen prior to ignition. The elimination of initial conditions has a negligible effect on hydrogen mass but reduces the air mass flow error from 1.7 to 0.6%.

The compression pressure is matched within 1%. Figure 14 compares the measured cylinder pressure with the results from 22 simulated cycles, with the pressure predicted from the first consecutive cycle removed. The simulated cycles are within CCV of the measured data. The 20 CPM cycles capture some of the CCV of the measured cylinder pressure. The authors are not claiming that 20 cycles are sufficient to accurately predict the CCV of cylinder pressure data for this case. Only 20 cycles were run due to computational resource limitations.

One of the CPM cycles with cylinder pressure close to the averaged experimental data, shown in Fig. 14, is selected for validating the apparent heat release rate (AHRR). Calculated AHRR using the maximum, minimum and mean

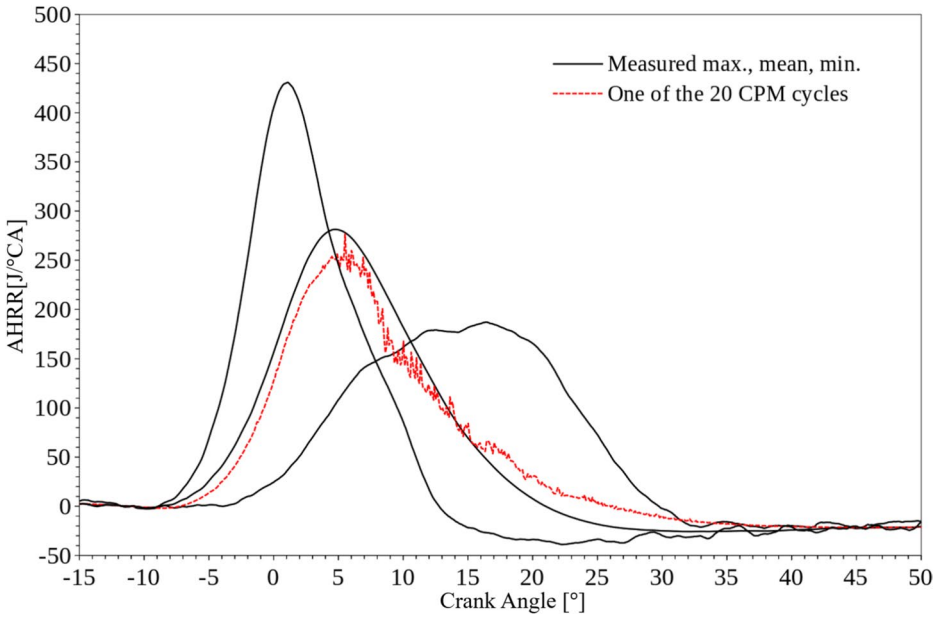

Fig. 15 AHRR of one CPM simulation calculated based on the measured and predicted cylinder pressures

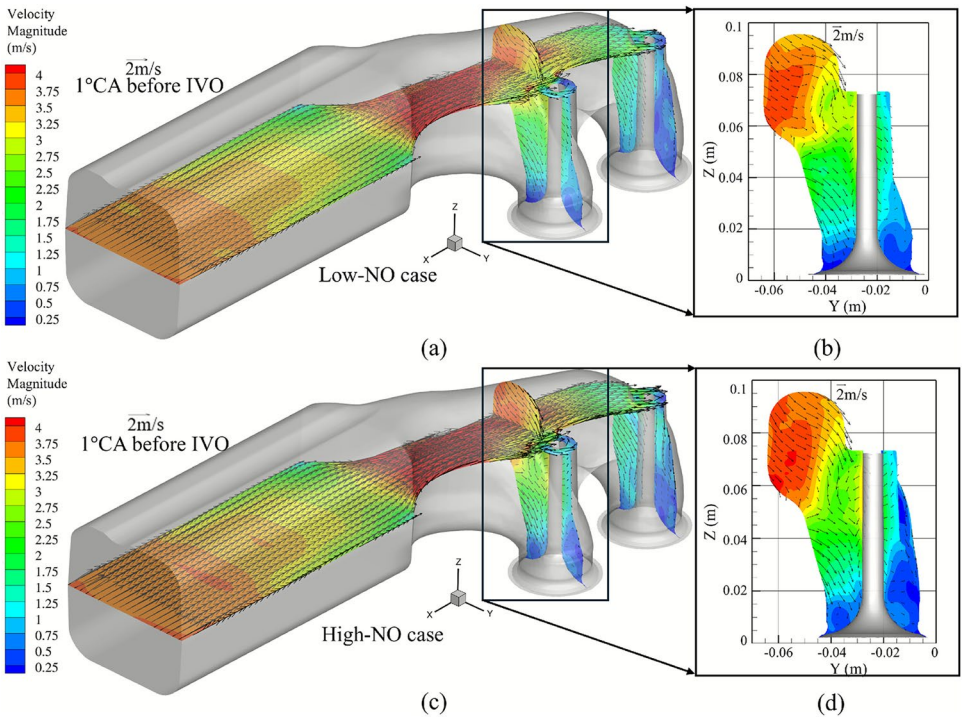

Fig. 16 Velocity contour inside the intake port, 0.5°CA before IVO for low-NO cycle at **a** 3-dimensional view and **b** YZ cut plane, and for high-NO cycle, **c** 3-dimensional view, **d** YZ cut plane

measured cylinder pressure data, is compared with the calculated AHRR from the simulation cycle and is shown in Fig. 15. The slower predicted initial AHRR indicates weaker combustion at the beginning. Consequently, more fuel remains for combustion during the expansion stroke, resulting in a higher AHRR later in the cycle.

5.2 H_2 injection, mixing, and NO generation

Another two cycles - one predicting higher NO and the other predicting lower NO - are selected to examine the influence of air-H_2 mixing on in-cylinder NO formation. Both simulations were started after 2 consecutive cycles were run, so the results are not biased towards any assumed initial conditions. Figure 16 presents the velocity on three different cut planes at 1°CA before IVO for both cycles. The velocity near the intake valve seat is approximately 1 m/s in both

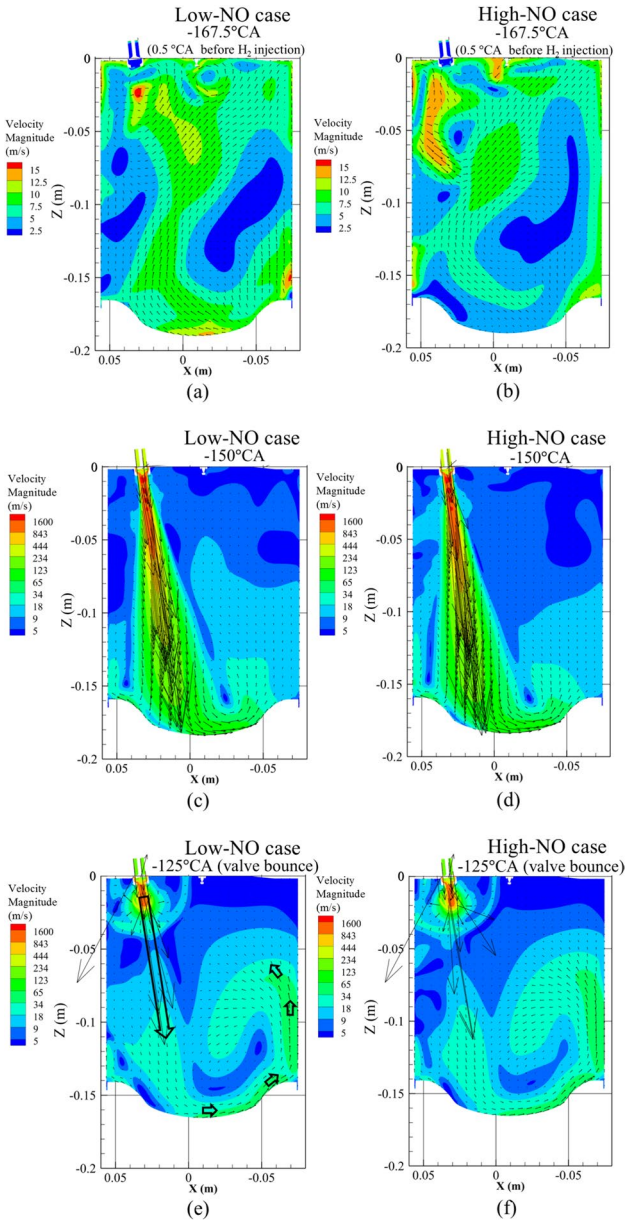

Fig. 17 Velocity contour at various crank angles during H_2 injection for low- and high-NO cycles at center xz plane of the cylinder

cases, and the overall flow fields exhibit similar patterns. The volume-averaged turbulent kinetic energy and turbulent velocity fluctuation within the intake port are 0.064 m^2/s^2 and 0.0196 m/s, respectively, for both cases. Nevertheless, local flow structures show noticeable differences. These small differences would be retained and allowed to grow when the intake valve opens due to high fidelity numerics (smaller cell sizes, smaller time steps and second order difference schemes) used.

The intake flow interacts with the flow inside the cylinder, forming distinct flow patterns between the low-NO and high-NO cycles right before H_2 injection, as shown

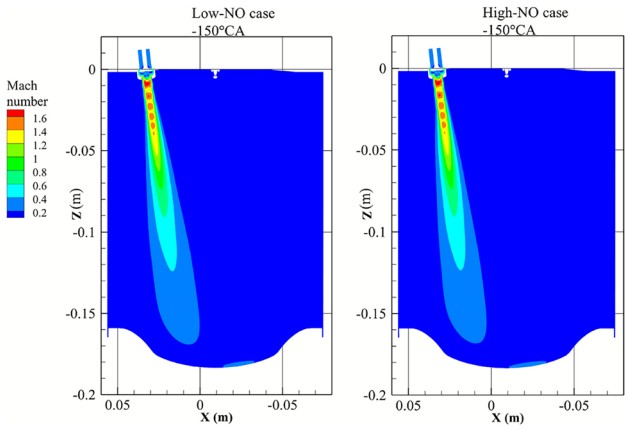

Fig. 18 Mach number contour at −150°CA for low and high-NO cycles, at the xz center plane of the cylinder

in Fig. 17a, b with the flow field displayed on the center xz plane of the cylinder. H_2 is injected into the cylinder at super-sonic speed, during the compression stroke, forming shock waves near the injector, as shown in Figs. 17c, d and 18. The highest speed is 1952 m/s, corresponding to a mach number of 1.9. The H_2 jet hits the piston, spreads along its surface, and gets deflected upwards along the liner wall, forming a large recirculation zone. The H_2 valve bounce sends in a second high-speed jet, facilitating the large recirculation zone formed by the first jet, as shown in Fig. 17e, f.

The deflected jets interact with the cylinder head at approximately –100°CA before top dead center for both low- and high-NO cycles, then move along the head toward the H_2 injector, as shown in Fig. 19a, b. In Fig. 19c–e, once the flow reaches the opposite side of the liner, it moves downward and forms a smaller secondary recirculation zone. As the piston rises, the flow primarily directs toward the spark plug, as illustrated in Fig. 19g, h at ignition timing. During this entire process, H_2 mixes with air. Poor mixing can create local H_2-rich pockets near the spark plug, which promotes high NO formation during combustion. Therefore, achieving a homogeneous mixture is critical for low emissions. In this paper, "H_2-rich" does not mean the local equivalence ratio is greater than 1. It only refers to a region of higher hydrogen concentration. To investigate the formation of H_2-rich pockets and their spatial relation to the spark plug in both low- and high-NO cycles, a horizontal plane 0.01 m ($z = -0.01$m) below the cylinder head is examined.

The flow patterns, developed from the small flow differences in the intake port during intake and compression strokes of these two simulations, can influence the behavior of the H_2 jet, particularly when the jet is deflected upward and its velocity decreases significantly. As a result, the jet impinges on the cylinder head closer to the exhaust valve (EV) side in the low-NO cycle, whereas it strikes nearer to

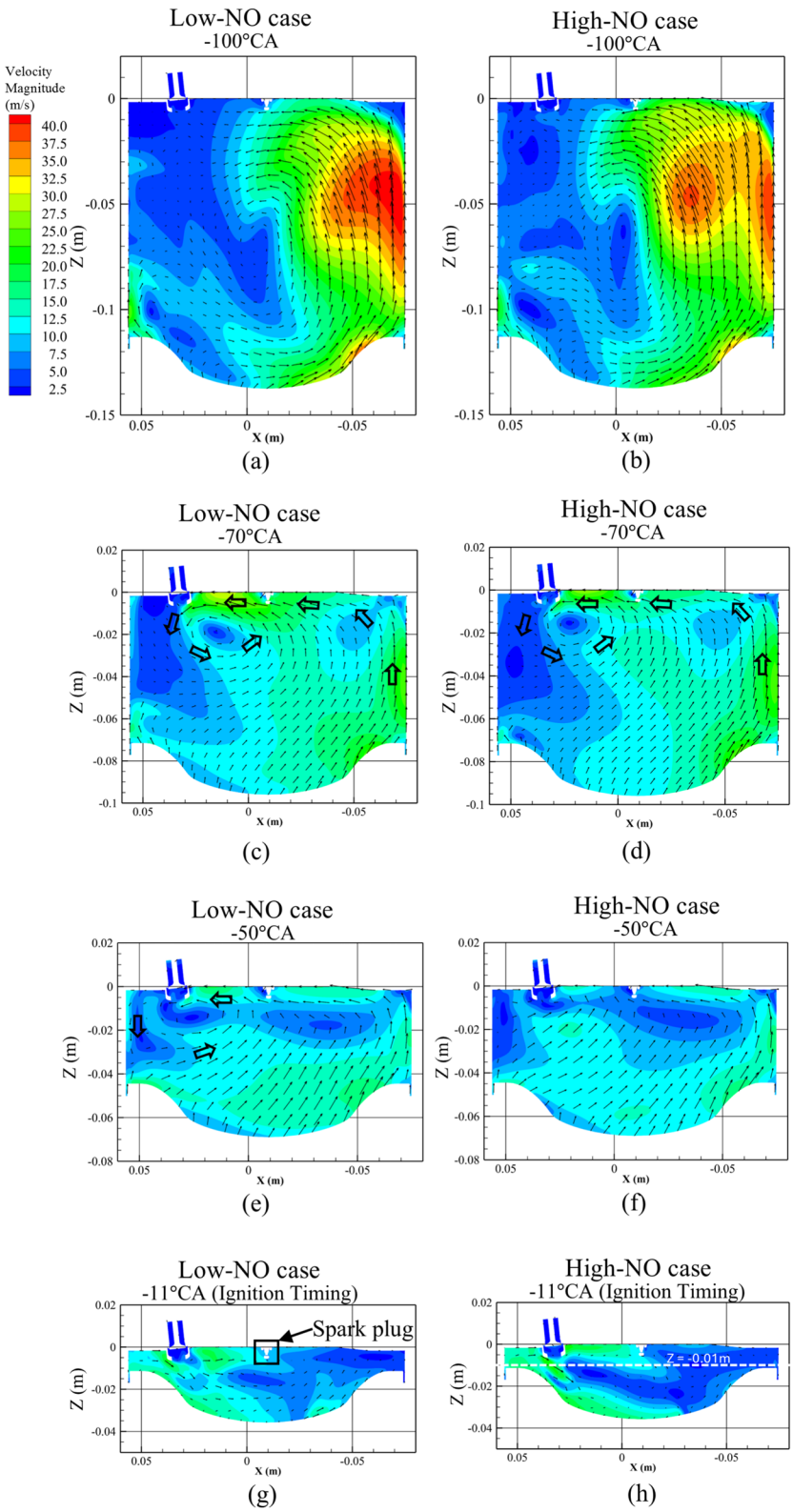

Fig. 19 Velocity contour at various crank angles throughout the rest of compression stroke for low- and high-NO cycles at center xz plane of the cylinder

the center in the high-NO cycle, as indicated by the velocity vectors in Fig. 20a, b.

The flow velocity toward the EV side is higher in the low-NO cycle, while it is more evenly distributed between the IV and EV sides in the high-NO cycle. A similar trend can be observed in the H_2 distribution contours. Once the upwards moving jet after deflecting off of the piston impinges on the cylinder head, the H_2 spreads across the

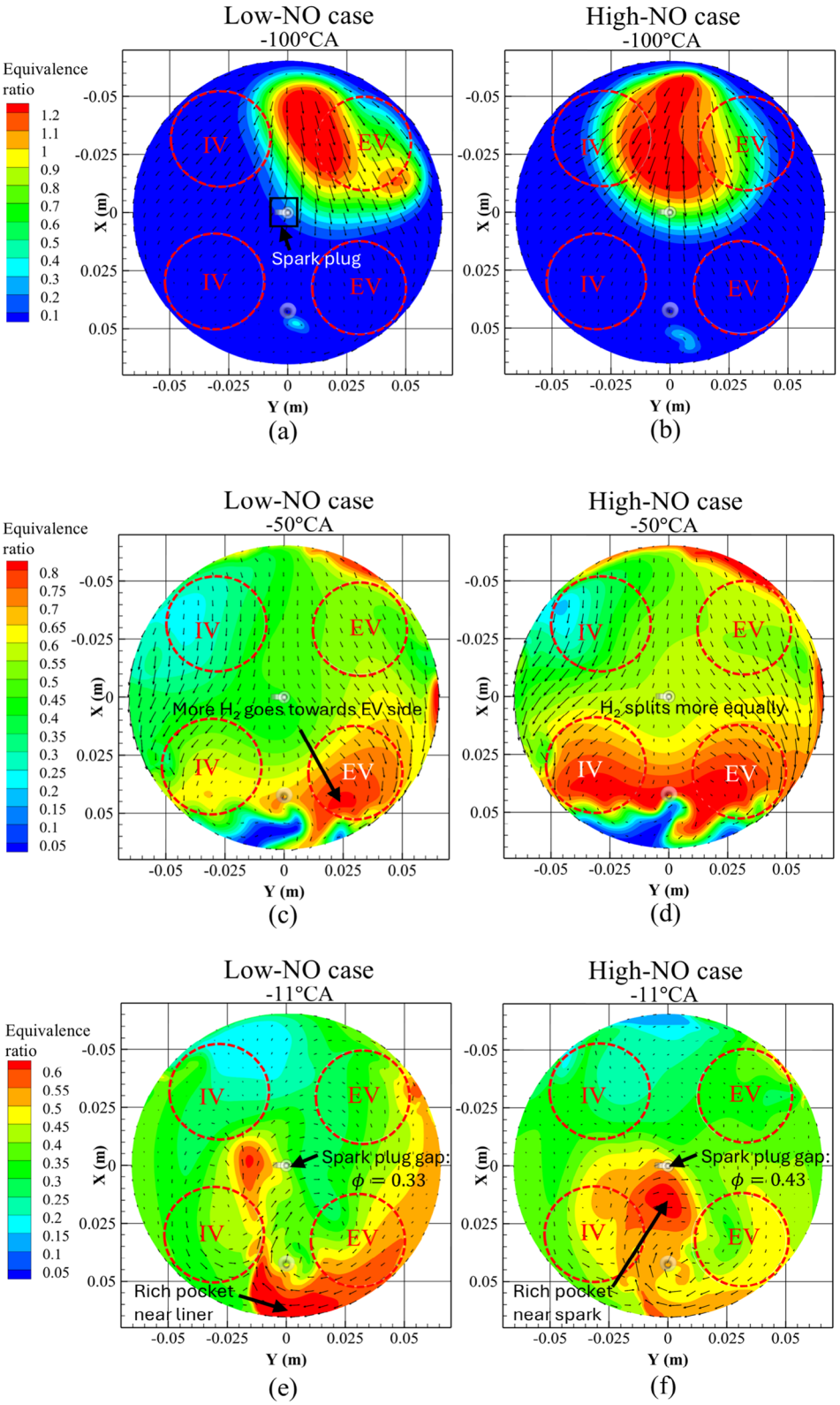

Fig. 20 Equivalence ratio at $z = -0.01$m plane during compression stroke and before ignition timing for low- and high-NO cycles

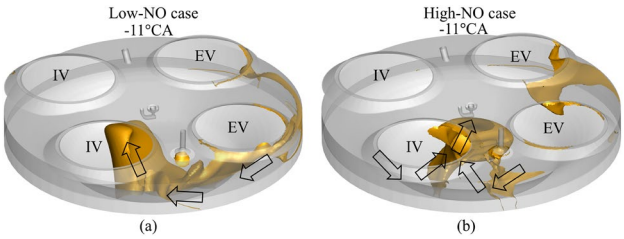

Fig. 21 Iso-surface with $\phi = 0.55$ at -11°CA

head toward the opposite side. At $-50\,^{\circ}$CA, before reaching the far side of the liner, most of the H_2 in the low-NO cycle remains concentrated on the EV side, whereas the H_2 distribution is more uniform in the high-NO cycle, as shown in Fig. 20c, d.

As shown in Fig. 19c–h, the small recirculation zone, indicated by the arrows, carries H_2 downward and then toward the spark plug. In the low-NO cycle, the H_2 concentrated on the EV side flows downward along the liner and piston, merges with the recirculation on the IV side, and then moves upward again, forming H_2-rich pockets near the liner, piston wall, and the backside (-y side) of the spark plug at ignition timing, as shown in Fig. 20e. In the high-NO cycle, the more evenly distributed H_2 from both the IV and EV sides flows downward, converges near the center, and then moves upward again, creating an H_2-rich pocket that travels toward the spark plug at ignition timing, as shown in Fig. 20f. The equivalence ratios (ϕ) at the spark plug gap are 0.33 and 0.43 for the low- NO and high-NO cycles, respectively. The iso-surface of $\phi = 0.55$ with flow directions shown in Fig. 20 show a more comprehensive picture of this process (Fig. 21).

Figure 22 shows the flame front evolution, represented by a 1200 K iso-surface colored by the local equivalence ratio, at different crank angles. After ignition, the flame kernel

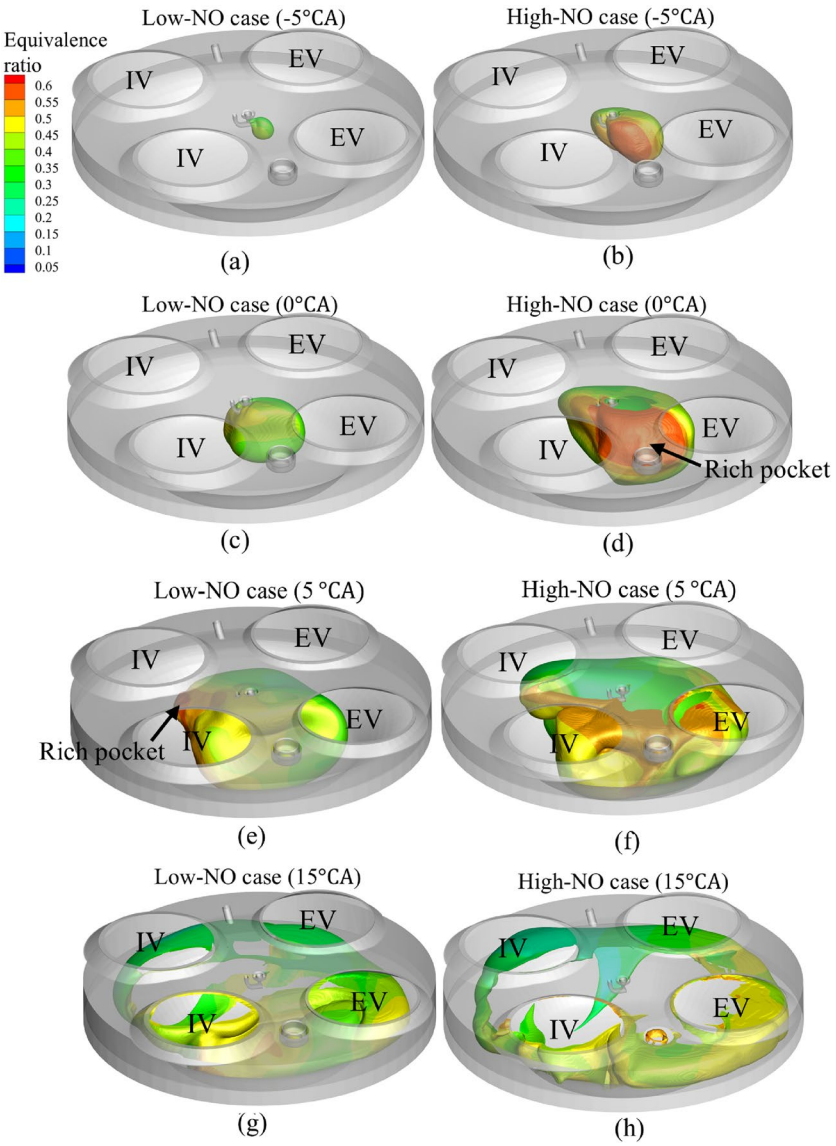

Fig. 22 Iso-surface with 1200 K temperature colored by equivalence ratio during combustion

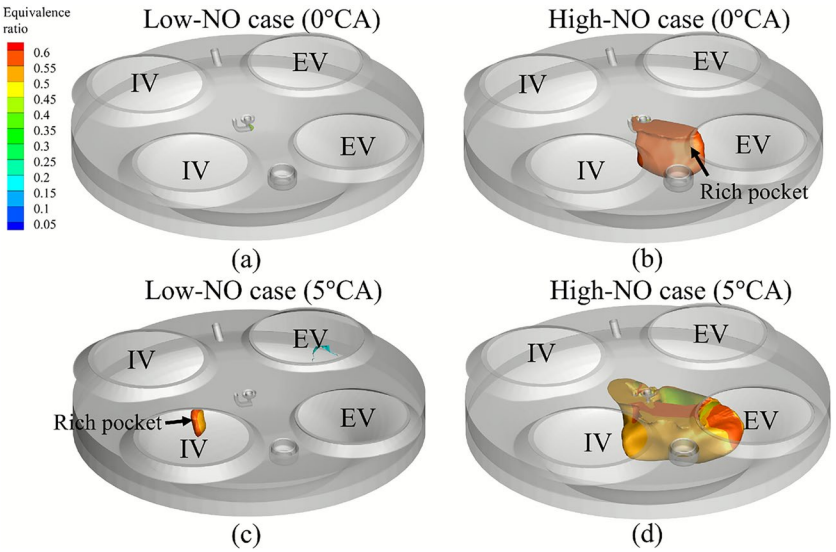

Fig. 23 Iso-surface with 50ppm NO concentration colored by equivalence ratio

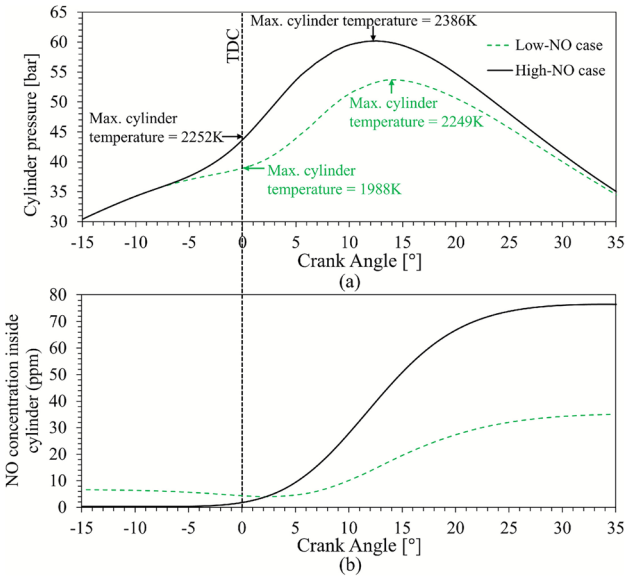

Fig. 24 Cylinder **a** pressure and **b** NO concentration for low-NO and high-NO cycles

initially grows toward the EV side, as seen in Fig. 22a, b. The growth is significantly faster in the high-NO cycle due to the richer mixture near the spark plug. The turbulent flame speeds estimated from the iso-surface evolution during the first 6 °CA after ignition are approximately 11.3 m/s and 21.8 m/s for the low- and high-NO cycles, respectively. As shown in Fig. 22b, d, the flame front encounters H_2-rich pockets immediately after ignition in the high-NO cycle, whereas in the low-NO cycle, this occurs only around 5 ° CA when the flame propagates toward the IV side. Based on experimental data, about 90% of the fuel is burned within 15 °CA for most cycles, so showing contours beyond this point is not necessary. The simulation results (Fig. 22g, h) indicate that combustion at this time primarily occurs near the wall.

Figure 23 presents the 50 ppm NO iso-surface colored by the local equivalence ratio at various crank angles. NO formation primarily occurs in the fuel-rich regions. In the high-NO cycle, NO is produced much earlier due to the presence of richer pockets near the ignition site, whereas in the low-NO cycle, significant NO formation appears mainly after 5 °CA, when the flame reaches the IV side where rich pockets are located.

Figure 24 shows the volume-averaged pressure and NO concentration inside the cylinder of the low and high-NO cycles. The near-ignition rich pockets in the high-NO cycle leads to faster combustion and higher in-cylinder pressure. The maximum temperature of the high-NO cycle is constantly higher than the temperature in the low-NO cycle by 264 K at TDC and 137 K at peak-pressure time. This higher temperature facilitates the generation of NO. As a result, at 35 °CA after top dead center, low and high-NO cycles have 32 ppm and 76 ppm NO, respectively.

5.3 NO emission in exhaust port

In experiments, the NO generated in cylinder flows into the exhaust port after EVO and was measured by a capillary probe positioned at the center of the exhaust duct and 10 mm from the outlet in Fig. 9. The probe has an inner diameter of 0.254 mm. To enable meaningful comparison with the experimental results, a monitor point was placed at the same location in the simulation. To match the probe's sampling area, the monitor point was defined as a cube with dimensions of 0.225 mm on each side. The mesh surrounding the monitor point was locally refined to 0.125 mm, and the volume-averaged NO concentration was recorded over time. The previous engine experiments as well as the

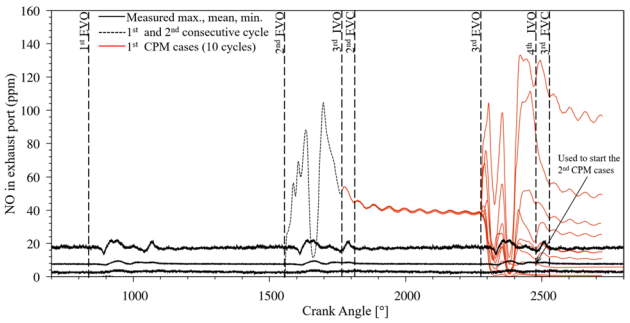

Fig. 25 NO concentration in the exhaust port from consecutive cycles and 1st CPM cases vs. experimental data

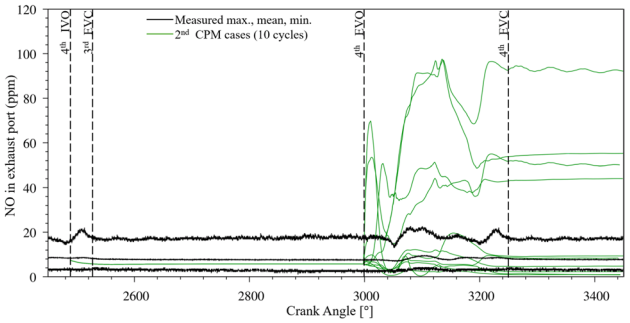

Fig. 26 NO concentration in the exhaust port from 2nd CPM cases versus experimental data

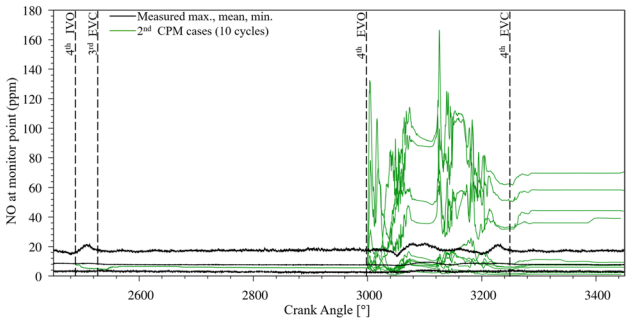

Fig. 27 NO concentration at the monitor point from 2nd CPM cases versus experimental data

Fast-NO measurement setup was already presented in [28]. All simulated cycles are setup to predict NO emissions with SAGE detailed chemistry model.

Figure 25 shows the NO concentration in the exhaust port from the consecutive cycles and the first 10 CPM cycles, compared with experimental data. Before the second EVO, the NO concentration is nearly 0 ppm due to the initial conditions. After the second EVO, NO formed inside the cylinder at high temperatures begins to flow into the exhaust port, causing the concentration to rise. The sudden drop in NO concentration between the second EVO and third IVO is caused by backflow at the engine outlet, which dilutes the NO concentration. As the simulation progresses, the effect of backflow is gradually diminished by the sustained flow from the cylinder.

Starting from the solution at the third IVO, 10 CPM cycles are initiated with an isotropic velocity perturbation applied throughout the intake port. Between the third IVO and the second exhaust valve close (EVC), the NO concentration decreases. However, the decline becomes more gradual, and all 10 cycles exhibit similar NO levels after the second EVC until the third EVO, due to the absence of any incoming combustion-chamber flow. This indicates that the NO concentration reaches a quasi-steady state between EVC and the subsequent EVO which is also shown in the measurement data. As shown, the quasi-steady NO concentration from the combustion of the second consecutive cycle is $\sim$ 40 ppm, which is around twice the maximum value observed in the experimental data, $\sim$ 20 ppm, possibly due to unreasonable H_2-rich pockets formed during the mixing process.

To investigate the influence of initial conditions on NO predictions on subsequent CPM cycles, a CPM cycle with NO closest to the experimental mean is selected to initiate the second set of 10 CPM cases, as indicated by the arrow in Fig. 25. The results are presented in Fig. 26. These 10 CPM cycles exhibit a similarly wide distribution of NO concentrations, suggesting that the initial NO level does not significantly impact the final results.

As shown in Fig. 27, due to turbulent flow and non-uniform NO distribution, the NO concentration at the monitor point exhibits more fluctuations than that in the whole of exhaust port. After the fourth EVC, the NO concentration quickly reaches a steady state, showing a slightly narrower range and distribution to that in the exhaust port, and with more stable values.

Although the predicted NO concentrations span a wider range than the experimental data, several simulated profiles quantitatively match the experimental trend: the NO level drops slightly immediately after EVO, then rises and fluctuates before gradually reaching a steady state after EVC. In other CPM cases, a significant rise in NO concentration occurs right after EVO, as a result of incoming larger amount of NO generated in the cylinder due to possible H_2 -rich pockets near the spark plug, as explained in Sect. 5.3. Nevertheless, the subsequent NO fluctuation still qualitatively aligns with the general behavior observed in the experimental data.

The occurrence of H_2-rich pockets and the resulting high NO concentrations is likely caused by the use of the unsteady RANS turbulence model, which leads to insufficient H_2-air mixing within the cylinder, which has been reported before [29, 30]. In contrast, the Large Eddy Simulation (LES) turbulence model can capture transient small-scale eddies, enhancing mixing by disrupting fuel-rich pockets and promoting diffusion. Future work will therefore

look into the use of LES models to resolve cylinder motion and fuel-air mixing.

6 Conclusion and discussion

In this work, we present a computational model for hydrogen injection and combustion in an IC engine that involves the injector needle motion. The studied injector is the *Bosch* F2 hydrogen injector, an early prototype of the hydrogen injector series by *Bosch*. Comparisons with experimentally measured cylinder pressure and exhaust NO data are done to validate the computational setup. The injector needle bounce effect is incorporated into the needle motion profile, leading to more realistic predictions of hydrogen-air mixing.

The computational model predicts the inflow air and injected hydrogen mass within 0.6% and 1.4% against measurement data, respectively. The cylinder compression pressure prior to ignition is only 0.7% lower than the measured pressure. Across 22 simulated cycles, the cylinder pressure remains roughly within the measured range of the experimental data. CPM is used to obtain multiple simulation cycles at a lower computational cost.

A clear correlation between hydrogen-rich pockets, high-temperature regions, and NO formation is revealed by analyzing the in-cylinder conditions of two representative cases corresponding to low and high NO mass. In this paper, "H_2 -rich" does not mean the local equivalence ratio is greater than 1. It only refers to a region of higher hydrogen concentration. The local H_2-rich pockets formed due to poor H_2-air mixing and their locations relative to the spark plug are crucial to NO formation in these cases analyzed. The low-NO case has the H_2 jet (deflected off the piston) hitting the EV side of the head, leading to local fuel rich pockets away from the spark plug; the high-NO case has the H_2 jet impinging the head more at the center, leading to H_2-rich pockets closer to the spark plug, faster combustion, higher maximum temperature, and significantly higher NO formation. This highlights the importance of accurately resolving the H_2-air mixing process.

Two consecutive cycles were simulated first to wash out the initial conditions. Then two sets of 10 CPM cycles were simulated by introducing an isotropic velocity perturbation inside the intake port at IVO. These minuscule velocity perturbations were sufficient to create different yet valid realizations of the intake flow fields which affected the combustion in a statistically similar way to that of consecutively run simulation cycles. Between each EVO and EVC, the NO concentration inside the exhaust port and at the monitor point was seen to fluctuate due to back flow at the outlet boundary and the new exhaust gases flowing in from the cylinder. After each EVC, the NO concentration gradually converges to a steady value.

The overall NO concentration range remains similar between the first and the second set of 10 CPM cycles showing that the NO predictions from CPM simulations are not biased on the cycle chosen to initiate CPM runs. This indicates that CPM by design produces statistically comparable results to that of consecutively run cycles regardless of the initial conditions, as long as the statistics are collected using a large enough number of CPM cycles.

The 20 CPM cycles show a wider range of NO distribution compared to the measured data, with some cycles overpredicting the NO concentration. It is important to interpret these results in the context of the turbulence modeling approach. While the unsteady RANS model inherently averages small-scale turbulent fluctuations, contributing to an overprediction of absolute NO levels due to underestimated micro-mixing, it successfully isolates the macroscopic cycle-to-cycle variability of the fuel distribution. The observed NO variations are primarily driven by the macroscopic deflection of the supersonic hydrogen jet, which dictates the transport of fuel-rich pockets relative to the spark plug. Consequently, the presented CPM-URANS framework proves effective for identifying system-level sensitivities to boundary dynamics, providing statistical insights that would be computationally prohibitive with LES.

In this work, only 20 CPM cycles are simulated due to constraints faced in the computational resources. To obtain statistically meaningful results at least 100 cycles are recommended in the literature which will be considered in a future study. However, the authors do not think running only 20 CPM cycles affected the qualitative results or the core conclusions of this study regarding the sensitivity of NO formation to boundary fluctuations.

Finally, the operating strategy investigated in this study utilized a lean-burn concept without Exhaust Gas Recirculation (EGR) and a reduced compression ratio to strictly isolate the effects of injection dynamics on mixture formation and to mitigate knock risks. While EGR is indispensable for modern heavy-duty applications to further reduce NO_x emissions, its exclusion in this fundamental study allows for a clear attribution of cycle-to-cycle variations to the injector-intake interaction. Future investigations will extend this methodology to include EGR, analyzing how residual gas transients interact with the identified mixing phenomena.

Acknowledgements The authors thank all contributors to this work. *Bosch* provided the early prototype F2 HIDI hydrogen injector and the corresponding valve lift data. *Volvo* supplied the D13 engine. Convergent Science provided CONVERGE licenses, computational resources and technical support for this work.

Author Contributions Marcel Reinbold (M.R.) designed the research, performed the numerical investigations, analyzed the data, and wrote

the manuscript. Mingyi Liang (M.L.) designed the research, performed the numerical investigations, analyzed the data, and wrote the manuscript. Manuel Bucherer (M.B.) designed the research, conducted the experimental work, analyzed the results, and wrote, reviewed, and edited the manuscript. Sameera Wijeyakulasuriya (S.W.) designed the research, analyzed the results, and reviewed and edited the manuscript. Thai An Bui (T.B.) performed the numerical investigations. Thomas Koch (T.K.) reviewed the manuscript. Kelly Senecal (K.S.) reviewed the manuscript.

Funding Open Access funding enabled and organized by Projekt DEAL.

Data Availability No datasets were generated or analysed during the current study.

Declarations

Conflict of interest Mingyi Liang and Sameera Wijeyakulasuriya are employees of Convergent Science, and Kelly Senecal is a co-founder and owern of Convergent Science, the developer of the CONVERGE CFD software used in this study. The software was used solely as a simulation tool for the numerical investigations. The involvement of these authors did not influence the study design, the analysis or interpretation of the results, nor the presentation of the findings. All analyses were conducted objectively, and no results were modified or selected to favor the software or Convergent Science. All other authors declare that they have no Conflict of interest.

References

1. Convention on Climate Change United Nations Framework. Paris Agreement (2015)
2. Convention on Climate Change United Nations Framework. Glasgow Climate Pact (2021)
3. European Environment Agency. Treibhausgasemissionen nach Quellsektor ENV_air_ GGE__custom_1256039
4. Klell, M., Eichlseder, H., Trattner, A.: Wasserstoff in der Fahrzeugtechnik. Springer Fachmedien Wiesbaden, Wiesbaden (2018)
5. Brauer, M., Maaß, J., von Römer, L., Riess, M.: Optimization of the mixture formation in DI hydrogen combustion engines by modified injector nozzle design (2022)
6. Bifen, W., Torelli, R., Pei, Y.: Numerical modeling of hydrogen mixing in a direct-injection engine fueled with gaseous hydrogen. Fuel **341**, 127725 (2023)
7. Zareei, J., Rohani, A., Mahmood, W.M.F.W.: Simulation of a hydrogen/natural gas engine and modelling of engine operating parameters. Int. J. Hydrog. Energy **43**(25), 11639–11651 (2018)
8. Scarcelli, R., Wallner, T., Salazar, V.M., Kaiser, S.A.: Modeling and experiments on mixture formation in a hydrogen direct-injection research engine. SAE Int. J. Engines **2**(2), 530–541 (2009)
9. Babayev, R., Andersson, A., Dalmau, A.S., Im, H.G., Johansson, B.: Computational characterization of hydrogen direct injection and nonpremixed combustion in a compression-ignition engine. Int. J. Hydrog. Energy **46**(35), 18678–18696 (2021)
10. Sukumaran, S., Kong, S.-C.: Numerical study on mixture formation characteristics in a direct-injection hydrogen engine. Int. J. Hydrog. Energy **35**(15), 7991–8007 (2010)
11. Ameen, M.M., Yang, X., Kuo, T.-W., Som, S.: Parallel methodology to capture cyclic variability in motored engines. Int. J. Engine Res. **18**(4), 366–377 (2017)
12. Probst, D.M., Wijeyakulasuriya, S., Pomraning, E., Kodavasal, J., Scarcelli, R., Som, S.: Predicting cycle-to-cycle variation with concurrent cycles in a gasoline direct injected engine with large eddy simulations. J. Energy Res. Technol. **142**(4), 042202 (2020)
13. Bucherer, M., Reinbold, M., Bui, T.A., Kubach, H., Koch, T.: Mixture formation and corresponding knock limits in a hydrogen direct injection engine using different jet forming caps, p. 2024–01–2113 (2024)
14. Szpica, D.: Comparative analysis of the characteristics of a low-pressure gas-phase injector. Flow Meas. Instrum. **58**, 74–86 (2017)
15. Munson, B.R., Okiishi, T.H., Huebsch, W.W., Rothmayer, A.P.: Fundamentals of Fluid Mechanics, 7th edn. Wiley, Hoboken (2013)
16. Richards, K.J., Senecal, P.K., Pomraining, E.: CONVERGE 3.0 manual. Technical report (2023)
17. Yakhot, V., Orszag, S.A.: Renormalization group analysis of turbulence. I. Basic theory. J. Sci. Comput. **1**(1), 3–51 (1986)
18. Issa, R.I.: Solution of the implicitly discretised fluid flow equations by operator-splitting. J. Comput. Phys. **62**(1), 40–65 (1986)
19. Redlich, O., Kwong, J.N.S.: On the thermodynamics of solutions. V. An equation of state. Fugacities of gaseous solutions. Chem. Rev. **44**(1), 233–244 (1949)
20. Amsden, A.A., O'Rourke, P.J., Butler, T.D.: A computer program for chemically reactive flows with sprays. Technical Report LA-11560-MS, 6228444 (1989)
21. Launder, B.E., Spalding, D.B.: The numerical computation of turbulent flows. Comput. Methods Appl. Mech. Eng. **3**(2), 269–289 (1974)
22. Senecal, P.K., Richards, K.J., Pomraning, E.: Converge 4 manual. Convergent Science. Madison (2024)
23. Dong, S., Wagnon, S.W., Maffei, L.P., Kukkadapu, G., Nobili, A., Mao, Q., Pelucchi, M., Cai, L., Zhang, K., Raju, M., Chatterjee, T., Pitz, W.J., Faravelli, T., Pitsch, H., Senecal, P.K., Curran, H.J.: A new detailed kinetic model for surrogate fuels: C3MechV3.3. Appl. Energy Combust. Sci. **9**, 100043 (2022)
24. Senecal, P.K., Pomraning, E., Richards, K.J., Briggs, T.E., Choi, C.Y., McDavid, R.M., Patterson, M.A.: Multi-dimensional modeling of direct-injection diesel spray liquid length and flam lift-off length using CFD an parallel detailed chemistry
25. Coffee, T.P., Heimerl, J.M.: Transport algorithms for premixed, laminar steady-state flames. Combust. Flame **43**, 273–289 (1981)
26. Pal, P., Kolodziej, C., Pomraning, E., Probst, D., Wijeyakulasuriya, S.: Accelerating computational fluid dynamics simulations of engine knock using a concurrent cycles approach. In: Proceedings of the ASME 2020 Internal Combustion Engine Fall Technical Conference (2020)
27. Daw, C.S., Wagner, R.M., Drallmeier, J.A.: Characterization of lean combustion instability in premixed charge spark ignition engines. Int. J. Engine Res. **1**, 301–320 (2000)
28. Bucherer, M., Schmid, H.F., Lanzer, T., Kubach, H., Koch, T.: Fast-NO emission analysis of different mixture formation

strategies in a hydrogen single-cylinder heavy-duty engine. Automot. Engine Technol. **10**(1), 9 (2025)
29. Wang, Y., Kabil, I., Xu, C., Scarcelli, R., Cantrell, B., Anders, J., Wijeyakulasuriya, S.: Assessing model sensitivities for predictive CFD simulations of a h2-fueled off-road internal combustion engine. ICEF2025, ASME2025 (2025)
30. Wang, Y., Scarcelli, R., Bestel, D., Demir, S., Srna, A.: Multidimensional modeling of mixture formation in a hydrogen-fueled heavy-duty optical engine with direct injection. J. Eng. Gas Turbines Power **147**(9), 091011, 01 (2025)